Catalytic Oxidation of Volatile Organic Compounds Alone or in Mixture over Mg4Al2-xCex Mixed Oxides

F. Sahraoui, N. Haddad, Jean-Francois Lamonier, C. Rabia

catalysts

MDPI

Article

Catalytic Oxidation of Volatile Organic Compounds Alone or in Mixture over $Mg_4Al_{2-x}Ce_x$ Mixed Oxides

Faiza Sahraoui [1], Naima Haddad [1,*], Jean-François Lamonier [2,*] and Chérifa Rabia [1]

[1] Laboratory of Chemistry of Natural Gas, Faculty of Chemistry, University of Sciences and Technology Houari Boumediene, BP 32, Algiers 16111, Algeria
[2] Univ. Lille, CNRS, Centrale Lille, Univ. Artois, UMR 8181—UCCS—Unité de Catalyse et Chimie du Solide, F-59000 Lille, France
* Correspondence: akrour_naima@hotmail.com (N.H.); jean-francois.lamonier@univ-lille.fr (J.-F.L.); Tel.: +213-21-24-79-64 (N.H.)

Abstract: This study investigates Ce-containing MgAl layered double hydroxides (LDH), focusing on its structural and catalytic properties. $Mg_4Al_{2-x}Ce_x$ (x = 0; 0.4; 0.8; 2) hydrotalcite-like compounds were prepared using the co-precipitation method. The effects of cerium content and calcination temperature on the structural and catalytic properties of Ce-containing MgAl LDH were investigated. The samples were characterized by XRD, BET, Raman, XPS, and DTA/TGA techniques. The catalytic activity of the resulting compound in *n*-butanol oxidation was studied. Increasing the calcination temperature (from 280 to 500 °C) caused changes in the structural, textural, and reducibility properties. The $Mg_4Al_{2-x}Ce_x$ LDH structure series (calcined at 280 °C) exhibited the highest catalytic activity, especially for x = 2. The material's properties improved with increased Ce content, allowing complete butanol conversion below 280 °C. The formation of active sites occupied by cerium within the LDH structure, along with its reducibility properties, contributed to the material's performance. The Ce^{3+}/Ce^{4+} redox couple in the external layers enhanced O^{2-} diffusion and their activation into nucleophilic species, facilitating butanol transformation. Adding water vapor to the reaction mixture slightly decreased the butanol oxidation, while the presence of ethyl acetate and butanol together exhibited a mutual inhibitory effect, with butanol demonstrating a more prominent influence.

Keywords: catalytic oxidation; *n*-butanol; hydrotalcite; cerium

Citation: Sahraoui, F.; Haddad, N.; Lamonier, J.-F.; Rabia, C. Catalytic Oxidation of Volatile Organic Compounds Alone or in Mixture over $Mg_4Al_{2-x}Ce_x$ Mixed Oxides. *Catalysts* **2023**, *13*, 1269. https://doi.org/10.3390/catal13091269

Academic Editors: Piotr Kuśtrowski and Young Dok Kim

Received: 21 June 2023
Revised: 24 August 2023
Accepted: 31 August 2023
Published: 3 September 2023

1. Introduction

The primary sources of air pollution are the release of volatile organic compounds (VOCs) from various industrial processes and vehicular emissions, which pose significant health risks to humans. To address this issue, catalytic oxidation has emerged as a viable solution for the complete elimination of VOCs. This technology operates at low temperatures and is cost-effective, producing carbon dioxide and water as the end products. Precious metals, metal oxides, and mixed metal oxides are commonly used catalysts for this method of VOCs removal [1–5]. Precious metals like platinum or palladium exhibit greater activity than metal oxide; however, they are costly and subject to sintering and poisoning [6]. The mixed oxides with transition metal cations have emerged as a promising category of solid catalysts. Among them, cerium oxide has been the focus of numerous studies due to its beneficial properties in oxidation catalysis [7–10]. Notably, a crucial property of ceria is its ability to serve as an oxygen reservoir, storing and releasing oxygen through a redox shift between Ce^{4+} and Ce^{3+}. It is well established that altering the synthesis route for catalyst preparation can significantly influence the dispersion of active metallic species, thereby impacting the activity trends for various reactions [11]. In recent years, layered double hydroxides (LDHs) have garnered increasing attention due to their adjustable chemical composition, high surface-to-volume ratios, rich availability of catalytically active sites, hierarchically porous layered structure, and strong electrostatic interaction between layers

and interlayer anions. LDHs have been utilized as both catalysts and catalyst precursors in various chemical reactions [5,7,12,13]. However, limited research has focused on the influence of calcination temperature on the structural evolution of hydrotalcite, which is the precursor to mixed metal oxides. Most studies have examined the oxides obtained from fully thermally decomposed hydrotalcite in various reactions, while research specifically investigating the preservation of the hydrotalcite structure and its impact on the reactivity of the solids remains scarce.

The synthesis of a cerium-based hydrotalcite and its application as a catalyst presents a fascinating opportunity to obtain a homogeneous material with cerium occupying specific sites. Despite the potential of this idea, there has been limited research focused on its development. Specifically, there have been very few studies that have partially substituted aluminum in MgAl hydrotalcite with cerium. Surprisingly, no existing literature has explored the physicochemical properties of a catalytic system based on magnesium and cerium within the hydrotalcite structure.

To further investigate this concept, valuable research can be conducted on the synthesis methods and characterization techniques required to achieve controlled cerium substitution in hydrotalcite-based materials. Exploring a range of calcination temperatures and reaction conditions would provide insights into determining the optimal parameters for obtaining the desired catalytic material. Therefore, the inclusion of cerium within the crystal lattice of layered double hydroxides can enhance lattice oxygen mobility, potentially leading to improved material activity. Moreover, utilizing LDHs as precursor materials offers an intriguing approach to generate mixed oxides capable of accommodating various bivalent and trivalent cations [14]. Furthermore, it would be crucial to examine the physicochemical properties of the resulting hybrid material, including its surface area, porosity, crystal structure, and catalytic activity.

The efficiency of transition metal-based catalysts in the oxidation of VOCs is contingent upon various factors, including the presence or absence of water in the reaction mixture and the nature of the pollutant under scrutiny [3,15–17]. As industrial emissions often contain a blend of VOCs with varying components, it is crucial to examine the catalytic behavior of catalysts in the oxidation of multicomponent VOC mixtures. The oxidation of VOC mixtures has been found to differ from that of single VOCs due to the interactions of the distinct species with the catalyst. The effects of VOC mixtures are challenging to anticipate a priori and typically result in an inhibiting effect [15–17]. Promoting effects are rarely observed, and changes in selectivity to by-products have been documented during the oxidation of VOC mixtures [15].

Despite the extensive research on the catalytic oxidation of various volatile organic compounds, there is a limited number of studies specifically addressing the catalytic total oxidation of *n*-butanol in air, whether alone [3,8,18] or in combination with other compounds [19,20]. It is worth noting that *n*-butanol and ethyl acetate are commonly encountered VOCs in the atmosphere, mainly due to their utilization as industrial solvents or biofuels, which increases the probability of their presence. Given their prevalence and potential environmental impact, it is crucial to explore efficient catalytic oxidation methods for the complete removal of *n*-butanol and other VOCs from the air.

The primary objectives of this study were (1) to investigate the impact of Ce^{3+} content doping into MgAl LDHs, (2) to compare the physico-chemical and catalytic activity of the original hydrotalcite-like compounds with their calcined products as catalysts in *n*-butanol combustion, and (3) to examine the inhibitory and/or promoting effects of water vapor and the *n*-butanol/ethyl acetate mixture on *n*-butanol combustion.

2. Results and Discussion

2.1. Characterization of Dried Samples

The X-ray diffraction (XRD) patterns for the $Mg_4Al_{2-x}Ce_x$-HT (x = 0, 0.4, 0.8, 2) precursors are shown in Figure 1, demonstrating a high degree of crystallinity and typical patterns of hydrotalcite-like compounds (Joint Committee on Powder Diffraction Standards

89-0460) for all samples. The presence of diffraction peaks at 2θ 11.6°, 23.4°, 34.8°, and 60.7°, corresponding to the crystallographic indices (003), (006), (012), and (110) and lattice distances d of 7.59 Å, 3.79 Å, 2.56 Å, and 1.52 Å, respectively, confirms the phase. However, the XRD patterns for the cerium-containing precursors ($Mg_4Al_{1.6}Ce_{0.4}$-HT, $Mg_4Al_{1.2}Ce_{0.8}$-HT, and Mg_4Ce_2-HT) demonstrated lower crystallinity compared to the precursor without cerium (Mg_4Al_2-HT), which was likely due to the ionic radii differences (Mg^{2+} 0.86 Å, Al^{3+} 0.67 Å, and Ce^{3+} 1.02 Å) causing distortions in the layers due to octahedral coordination. Additionally, the precursors containing cerium exhibited extra diffraction peaks at 2θ ≈ 28°, 33°, 48° and 56° correspond to the (111), (200), (220) and (311) reflection of CeO_2 in cubic fluorite structure (ICDD-JCPDS files 34-0394). This is consistent with findings obtained by J.S. Valente [7], who reported that the presence of Ce resulted in the coexistence of both CeO_2 and hydrotalcite phases with increasing Ce content promoting the concentration of CeO_2 phase.

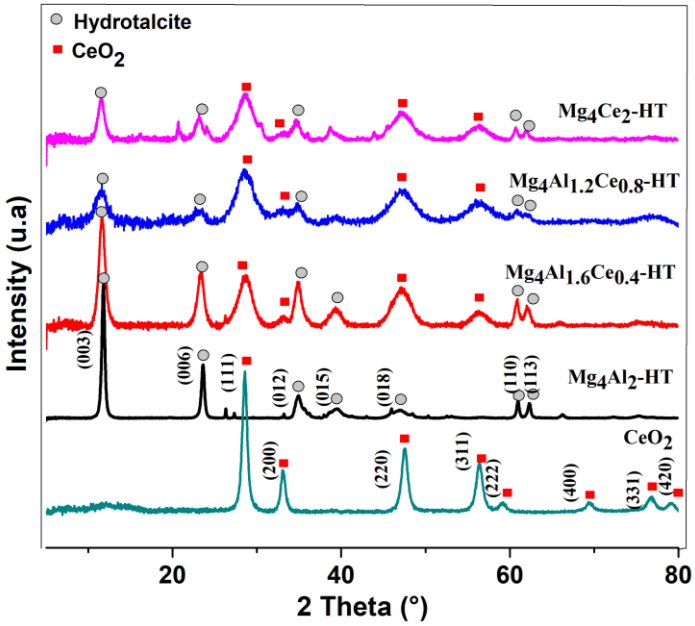

Figure 1. XRD patterns of $Mg_4Al_{2-x}Ce_x$-HT (x = 0, 0.4, 0.8, 2) precursors and commercial CeO_2 solids.

The cell parameters of the $Mg_4Al_{2-x}Ce_x$ (x = 0; 0.4; 0.8; 2) hydrotalcite phase was calculated assuming a 3R polytype with a hexagonal cell [21,22]. The lattice parameter a depends on the size of the cation in the brucite-like layers, which was calculated using the expression a = 2d (110), while parameter c is related to the distance between brucite-like layers, and it was obtained from the expression 1/2 [d(003) + 2d(006)] [23,24].

The results showed that increasing the amount of cerium in the samples is associated with an increase in lattice parameter a of the LDH. This can be attributed to the incorporation of Ce into the MgAl hydrotalcite material, as the larger ionic radius of Ce^{3+} caused an expansion in the cation–cation distance (Table 1).

Table 1. Lattice parameters of $Mg_4Al_{1-x}Ce_x$-HT solids.

Sample	Lattice Parameters	
	a (Å)	c (Å)
Mg_4Al_2-HT	3.03	22,73
$Mg_4Al_{1.6}Ce_{0.4}$-HT	3.04	22.79
$Mg_4Al_{1.2}Ce_{0.8}$-HT	3.05	23.00
Mg_4Ce_2-HT	3.05	23.00

The Raman spectra of $Mg_4Al_{2-x}Ce_x$-HT (x= 0; 0.4; 2) solids were found to be similar regardless of the particles observed except for differences in the relative intensity of certain lines. This indicates that in general, the same phases are present but with varying relative proportions. The Raman spectra of all the samples showed characteristic peaks attributed to the hydrotalcite phase for all the samples and to the CeO_2 phase for the cerium-containing materials ($Mg_4Al_{1.6}Ce_{0.4}$-HT and Mg_4Ce_2-HT). These findings are in line with the XRD data. The line at 1036 cm^{-1} was assigned to a "free" carbonate anion, which is not bonded to the brucite hydroxyl surface and water [25–27]. The line at 1055 cm^{-1} was attributed to carbonate anions bonded to the brucite hydroxyl surface, while the higher wavenumber line at 1079 cm^{-1} was attributed to carbonate anions that are strongly hydrogen bonded to water in the interlayer of hydrotalcite [26–28]. The line at 545 cm^{-1} was assigned to the symmetric stretching of M–O–M bonds in structural units of the LDHs [25,27]. In addition, for the two cerium-containing materials ($Mg_4Al_{1.6}Ce_{0.4}$-HT and Mg_4Ce_2-HT), an additional line at 451 cm^{-1} was observed, which was attributed to the F2g Raman active mode of the CeO_2 fluorite phase [28–30]. This line was similar to the one observed on the spectrum of commercial CeO_2 powder (as shown in Figure 2), but it was downshifted by 9 cm^{-1}, which was possibly due to a different chemical environment of CeO_2 in $Mg_4Al_{1.6}Ce_{0.4}$-HT and Mg_4Ce_2-HT compared to bulk CeO_2. This supports the assumption that Ce can be incorporated in the brucite-like octahedral layers, which is consistent with the XRD data.

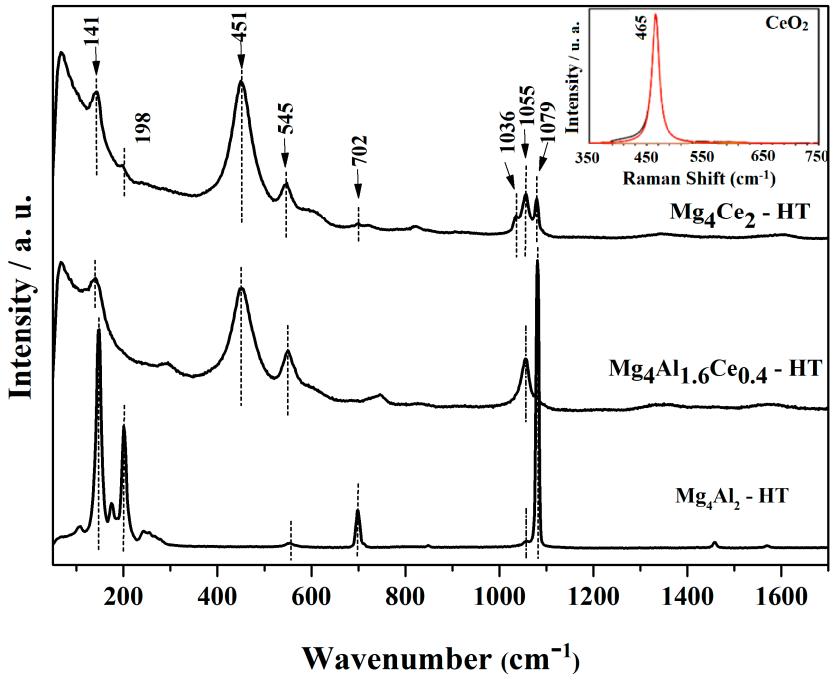

Figure 2. Raman spectra of $Mg_4Al_{2-x}Ce_x$-HT (x = 0, 0.4 and 2) precursors and commercial CeO_2.

The thermal decomposition In flowing air of the $Mg_4Al_{2-x}Ce_x$-HT (x= 0, 0.4 and 2) precursors was studied by simultaneous DTA/TG analyses (Figure 3). The first loss of mass in the temperature range 50–250 °C due to dehydration marked the thermal evolution of a hydrotalcite-like phase. This is attributed to the water molecules adsorbed on the surface of the double lamellar hydroxide as well as water located in the interfoliar domain [31–33]. This leads to the occurrence of an endothermic peak at around 200 °C. The second loss of mass is due to the loss of hydroxides in the form of water and decarbonation [14,31–33]. The DTA curves reveal that the dehydroxylation/decarbonation step, characterized by an endothermic signal around 380 °C, is associated with a low-intensity endothermic phenomenon around 317 °C and 307 °C for Mg_4Al_2-HT and $Mg_4Al_{1.6}Ce_{0.4}$-HT, respectively. This suggests that the dehydroxylation step occurs at a lower temperature for these two systems compared to Mg_4Ce_2-HT. However, even though the dehydroxylation step is slow

for Mg_4Ce_2-HT, this system is still the least thermally stable as its two decomposition peaks occur at lower temperatures than those observed for Mg_4Al_2-HT and $Mg_4Al_{1.6}Ce_{0.4}$-HT. The study's conclusion is that the layered structure of the three hydrotalcite-like compounds, Mg_4Al_2-HT, $Mg_4Al_{1.6}Ce_{0.4}$-HT, and Mg_4Ce_2-HT, does not collapse below 280 °C.

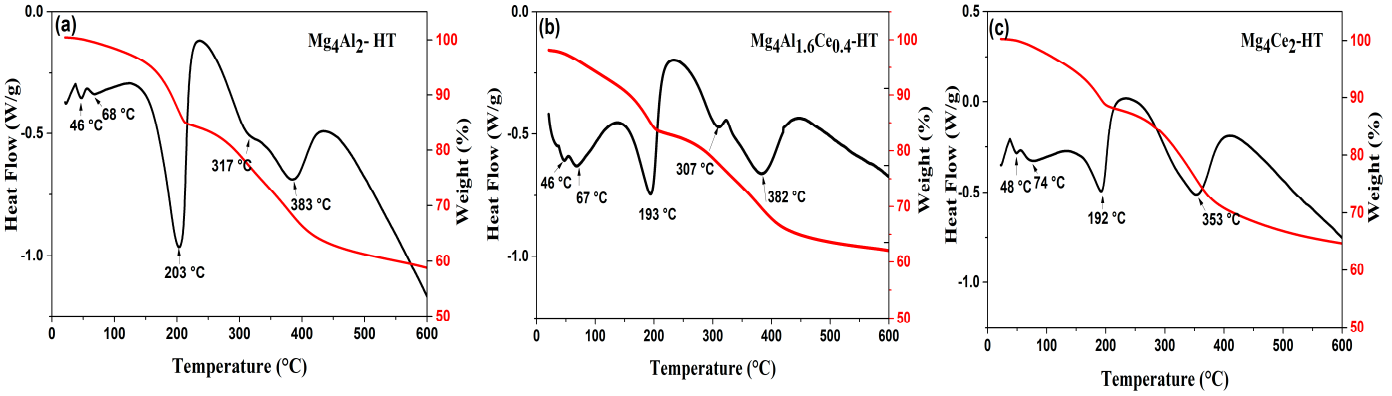

Figure 3. Differential thermal (black line) and thermogravimetric (red line) analyses (DTA/TG) profiles for the decomposition of (**a**) Mg_4Al_2-HT, (**b**) $Mg_4Al_{1.6}Ce_{0.4}$-HT and (**c**) Mg_4Ce_2-HT in air.

2.2. Characterization of Calcined Samples

To investigate the early stages of oxide phases crystallization, the dried samples are calcined at two temperatures 280 °C and 500 °C for 4 h in air. Following this, X-ray diffraction analysis is carried out with the diffractograms displayed in Figure 4. The resultant calcined samples were denoted as $Mg_4Al_{2-x}Ce_x$-HT280 and $Mg_4Al_{2-x}Ce_x$- HT500, where x stands for the Ce doping level (0, 0.4, 0.8 and 2).

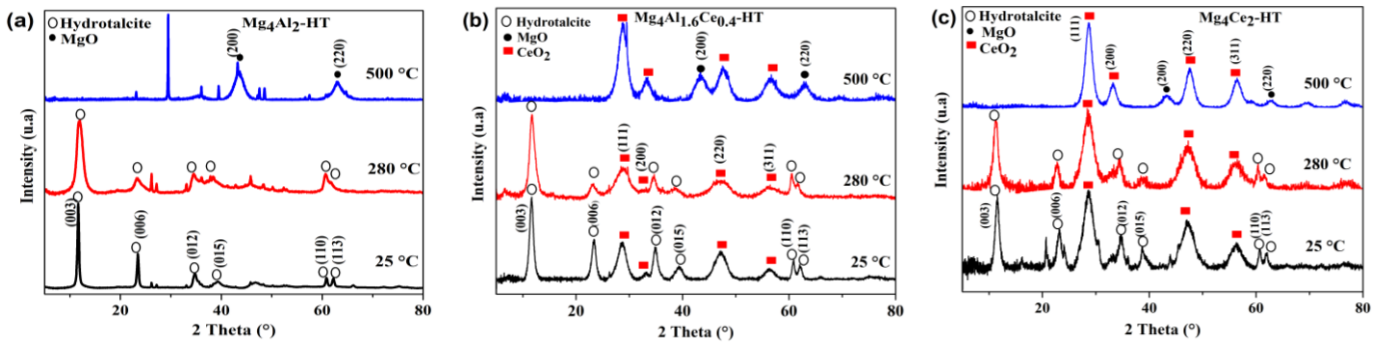

Figure 4. XRD patterns of (**a**) Mg_4Al_2-HT, (**b**) $Mg_4Al_{1.6}Ce_{0.4}$-HT and (**c**) Mg_4Ce_2-HT calcined at various temperatures.

The X-ray diffraction patterns of the three $Mg_4Al_{2-x}Ce_x$ (x = 0; 0.4 and 2) samples indicate that the LDHs structure remains partially stable until the temperature reaches 280 °C. At this temperature, there is a marginal reduction in intensity and broadening observed in the XRD patterns. Notably, the (003) peak, corresponding to the (003) plane, shifts modestly toward a smaller d-spacing (d ~ 0.1 Å) in comparison to the expected position of LDHs lines (JCPDS 89-0460). Simultaneously, the (003) and (006) diffraction lines of LDHs exhibit a slight decrease in intensity and broader profiles (Figure 5). This transformation can be attributed to the loss of physisorbed and interlayer water molecules, which are accompanied by a slight dehydroxylation of brucite-like sheets [7], as confirmed by the TGA/DTA analysis. A similar behavior has been documented by various researchers for LDHs containing (Mg, Al) [25,32,34]. These researchers suggested that the slightly weakened and broader XRD patterns of the calcined LDH sample, along with a subtle reduction in basal spacing (<1 Å), might be indicative of some structural disorder. Their conclusion was that the sample retains a partial layered structure, which is characterized by consistent metal–metal distances within the layers.

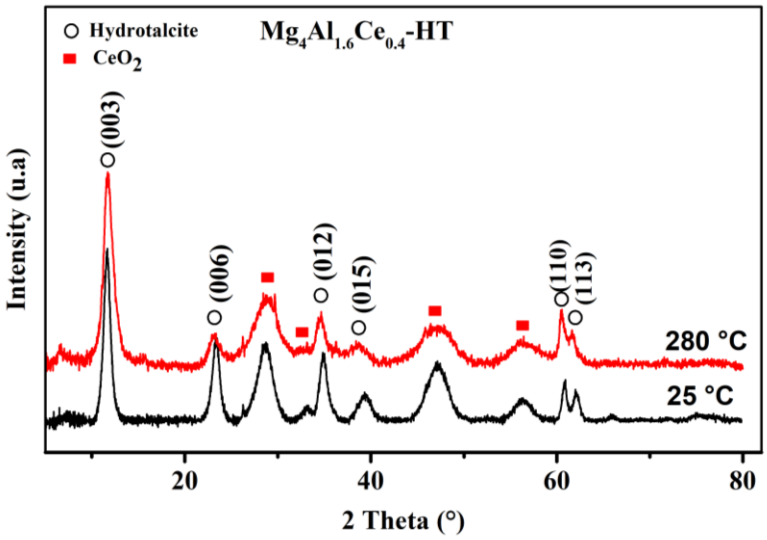

Figure 5. XRD patterns illustrating reduction in intensity of peaks and broader profiles in the $Mg_4Al_{1.6}Ce_{0.4}$-HT system during thermal treatment from 25 to 280 °C.

Upon further heating to 500 °C, the LDHs structure gradually decomposes, leading to the formation of MgO in a face-centered cubic structure (JCPDS Card No. 87-0653) and CeO_2 in a cubic fluorite structure (ICDD-JCPDS files 34-0394). Notably, aluminum oxide compounds are absent, which is possibly due to their transformation into an amorphous phase that supports the formation of the other oxides.

Table 2 presents the crystal sizes (L) of LDH, CeO_2, and MgO for samples synthesized and calcined at 280 °C and at 500 °C, as determined by the Scherrer equation. The results indicate that the as-synthesized sample without cerium (Mg_4Al_2-HT) exhibits a highly crystalline LDH phase, whereas the LDH crystallinity progressively diminishes with increasing cerium content. This reduction in LDH crystallite size implies that the LDH particles may have moved due to the additional interaction between the Ce and LDH particles upon Ce loading.

Table 2. Crystal sizes of as-synthesized and calcined samples determined by the Scherrer equation.

Sample	Hydrotalcite		CeO_2			MgO
	L_{003} (Å) [a]	L_{003} (Å) [b]	L_{111} (Å) [a]	L_{111} (Å) [b]	L_{111} (Å) [c]	L_{200} (Å) [c]
Mg_4Al_2-HT	183	54.6	-	-	-	29
$Mg_4Al_{1.6}Ce_{0.4}$-HT	93.6	67.6	26.8	26.1	37	34.9
Mg_4Ce_2-HT	72.7	75.6	30.1	32.1	49.5	39.5

[a] As-synthesized samples; [b] Calcined at 280 °C; [c] calcined at 500 °C.

During calcination at 280 °C, the LDH crystallinity decreased considerably for the Mg_4Al_2-HT and $Mg_4Al_{1.6}Ce_{0.4}$-HT samples, while it remained relatively unchanged for the Mg_4Ce_2-HT sample. Additionally, the CeO_2 crystals were smaller in $Mg_4Al_{1.6}Ce_{0.4}$-HT than in Mg_4Ce_2-HT (Table 2), and the MgO crystals were slightly larger in Mg_4Ce_2-HT. Based on these findings, we can conclude that the Mg_4Ce_2-HT system exhibited better crystallinity compared to the other two systems. These results are consistent with the TGA/DTA analysis, which showed that the Mg_4Ce_2-HT system was the least thermally stable and decomposed early, leading to better crystallization of the phases.

The textural characteristics of our elaborated systems vary depending on the cerium content and the calcination temperature. Figure 6 and Table 3 illustrate the N_2 adsorption–desorption isotherms, average pore diameters, specific surface area and pore volume for $Mg_4Al_{2-x}Ce_x$-HT280 and $Mg_4Al_{2-x}Ce_x$-HT500 samples.

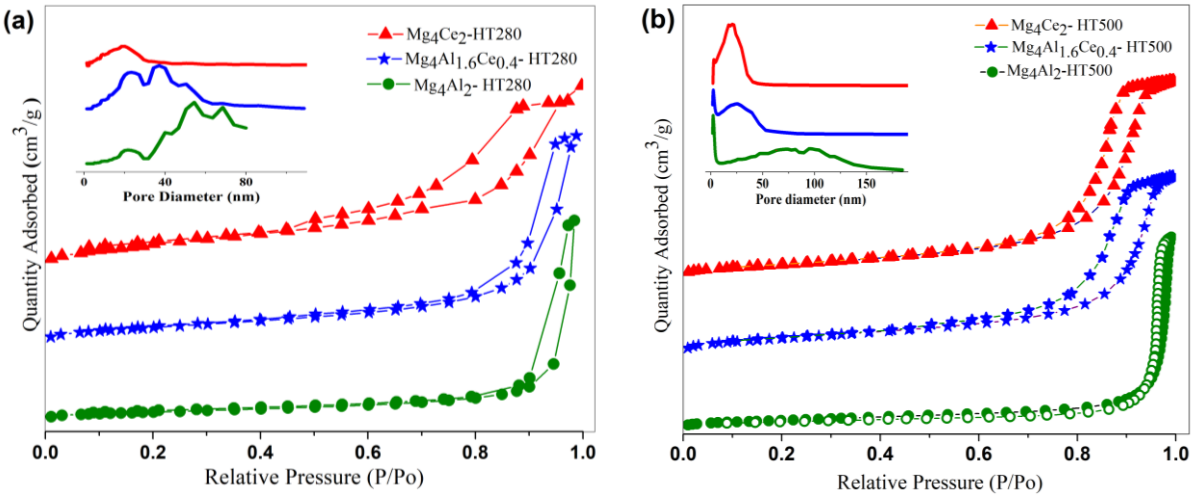

Figure 6. N_2 adsorption–desorption isotherms and the average pore diameters of (**a**) $Mg_4Al_{2-x}Ce_x$-HT280 (x = 0, 0.4 and 2) and (**b**) $Mg_4Al_{2-x}Ce_x$-HT500 (x = 0, 0.4 and 2).

Table 3. Surface area and pore volume of $Mg_4Al_{2-x}Ce_x$-HT after heat treatment at 280 °C and 500 °C.

Catalyst	S_{BET} (m^2/g)	Pore Volume (cm^3/g)
Mg_4Al_2-HT280	58.2	0.47
$Mg_4Al_{1.6}Ce_{0.4}$-HT280	112.5	0.46
Mg_4Ce_2-HT280	101.8	0.26
Mg_4Al_2-HT500	117.6	0.92
$Mg_4Al_{1.6}Ce_{0.4}$-HT500	84.2	0.31
Mg_4Ce_2-HT500	90.2	0.41

The nitrogen adsorption–desorption isotherms obtained regardless of the pretreatment temperature indicate that the cerium-containing systems, $Mg_4Al_{1.6}Ce_{0.4}$-HT and Mg_4Ce_2-HT, have type IV isotherms, which are characteristic of mesoporous solids. In contrast, the cerium-free system, Mg_4Al_2-HT, has a type II isotherm, indicating a strong presence of macropores. The pore distribution analysis using the BJH method confirms this texture difference between systems with and without cerium. The cerium-containing systems show a homogeneous pore distribution with a narrow peak at a diameter of about 30–40 nm, while the cerium-free system shows a wide peak at a diameter of about 60–100 nm, indicating the presence of macropores.

Regarding the measurement of surface area, there is a notable increase in the Ce-containing solids when the systems are pretreated at 280 °C. It increases from 58 m^2/g for the system without cerium to 101–112 m^2/g for the two systems containing cerium. The presence of cerium oxide and LDH phase at this temperature, as observed by XRD and Raman, leads to the development of porous materials. However, the trend is reversed when the pretreatment temperature is increased to 500 °C. In this case, the specific surface area decreases significantly from 117 m^2/g for Mg_4Al_2-HT500 to 84–90 m^2/g for the two systems $Mg_4Al_{1.6}Ce_{0.4}$-HT500 and Mg_4Ce_2-HT500. This decrease is explained by the complete collapse of the hydrotalcite phase, which leads to the destruction of micropores and a part of the mesopores structure, as well as more advanced crystallization of the cerium-based materials. This is in line with TGA/DTA analyses, which have shown that Mg_4Ce_2-HT solids are less thermally stable than cerium-free solids and decompose at a lower temperature, resulting in the formation of more highly crystallized oxides with larger crystallite size.

To obtain details about the chemical composition and states of the cerium species present on the surface, XPS analyses were conducted. Table 4 summarizes the data obtained from XPS analyses of $Mg_4Al_{1.6}Ce_{0.4}$-HT280 and Mg_4Ce_2-HT280 samples as well as for the catalysts (designated as $Mg_4Al_{1.6}Ce_{0.4}$-HT250 and Mg_4Ce_2-HT250) after the catalytic experiments, while Figure 7 depicts the O 1s and Ce 3d photopeaks for these two samples.

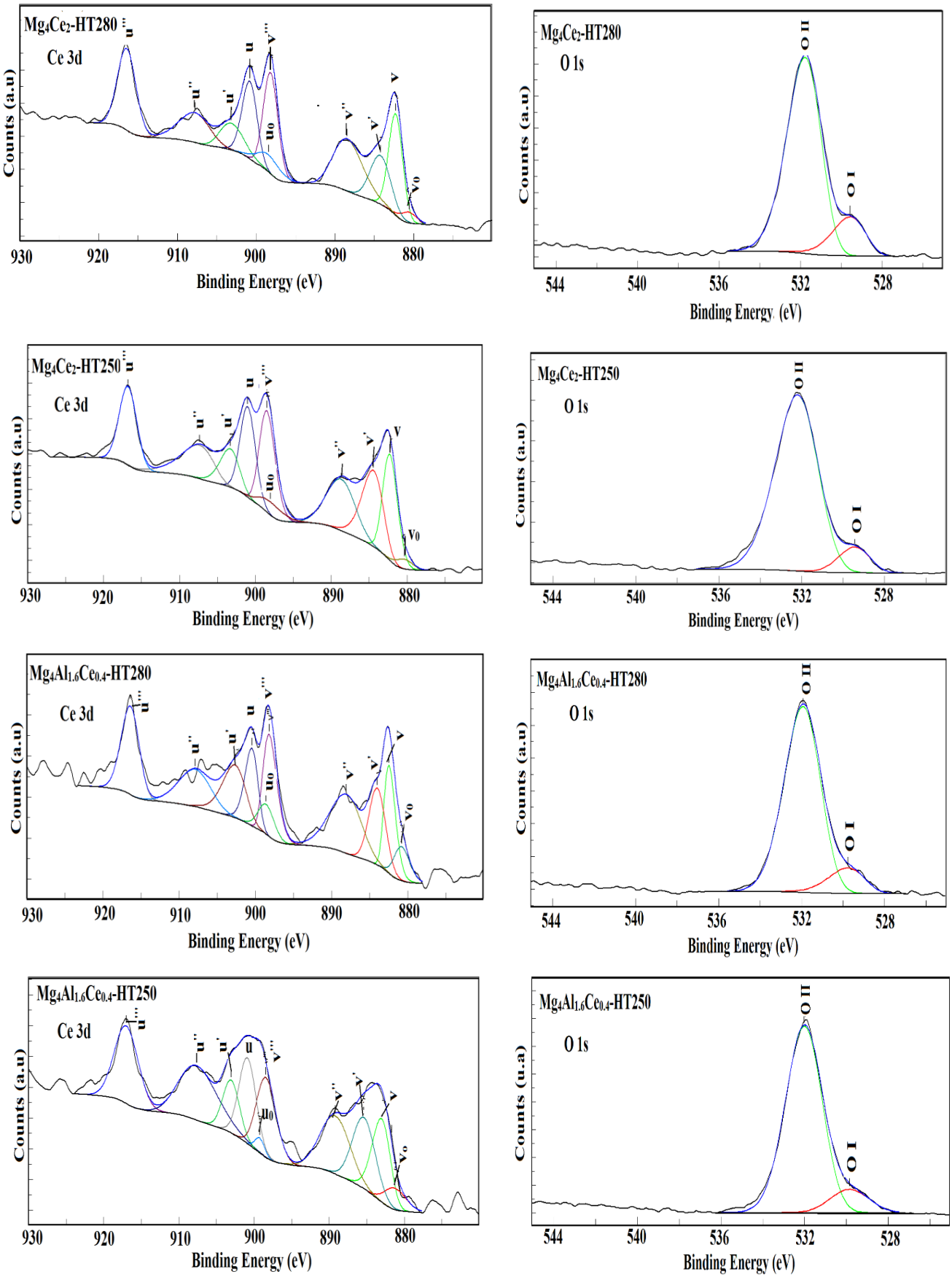

Figure 7. XPS spectra of Ce 3d and O 1s core levels in $Mg_4Al_{1.6}Ce_{0.4}$-HT and Mg_4Ce_2-HT samples calcined at 280 °C and tested at 250 °C.

Table 4. XPS analysis data of $Mg_4Al_{1.6}Ce_{0.4}$-HT and Mg_4Ce_2-HT samples obtained after calcination at 280 °C and following the catalytic test at 250 °C.

Sample	$Ce/(Ce+Mg)_{Bulk}$	$Ce/(Ce+Mg)_{XPS}$	O1s (BE)/eV		% u‴
			OI	OII	
$Mg_4Al_{1.6}Ce_{0.4}$-HT280	0.09	0.021	529.7	531.9	13.3
Mg_4Ce_2-HT280	0.33	0.020	529.5	531.7	14.7
$Mg_4Al_{1.6}Ce_{0.4}$-HT250	0.09	0.027	529.8	532.0	13.9
Mg_4Ce_2-HT250	0.33	0.049	529.4	532.2	12

The surface XPS values of Ce/(Ce +Mg), calculated from the area of the Ce 3d and Mg 1s core levels, are lower than the bulk ratio expected for the $Mg_4Al_{1.6}Ce_{0.4}$-HT280 and Mg_4Ce_2-HT280 samples (Table 4). This result indicates that Mg^{2+} and /or Al^{3+} ions are more dispersed on the surface than Ce^{3+} ions.

The O 1s core-level spectra were analyzed, and two peak contributions were identified as OI and OII components. The OI peak with a binding energy (BE) of 529.4–529.8 eV is associated with lattice oxygen [35,36]. On the other hand, the OII component with a BE of 531.7–532.2 eV can be attributed to surface-adsorbed oxygen (Oads), oxygen ions with low coordination states (O^{2-} and O^{-}), oxygen vacancies and oxygen atoms in hydroxyl or carbonate groups [36].

The relative proportion of Ce^{4+} present in the solid is assessed through the calculation of the percentage of the area under the Ce^{4+} u‴ (916.7 eV) relative to the total area under the Ce 3d spectral envelop using the method proposed by Shyu et al. [37]. The Ce 3d spectra of $Mg_4Al_{1.6}Ce_{0.4}$-HT280 and Mg_4Ce_2-HT280 samples show for both the systems the presence of mixed valence states of Ce^3+ and Ce^{4+}. However, the system with high cerium contents (Mg_4Ce_2-HT280) contains the largest proportion of Ce^{4+}, since the u‴ intensity goes from 13.3% to 14.7%. This correlation suggests an increase in the oxygen mobility in the solid with the cerium proportion, resulting in a decrease in the number of oxygen vacancies on the surface.

Furthermore, the reduction of Ce^{4+} to Ce^{3+} was more pronounced in the Mg_4Ce_2-HT250 catalyst after the catalytic test. This is evidenced by the decrease in intensity of the u‴ line from 14.7% to 12%, in contrast to the $Mg_4Al_{1.6}Ce_{0.4}$-HT250 catalyst, where the u‴ line intensity remained relatively stable. These results suggest that the Mg_4Ce_2-HT280 system has higher reducibility than the $Mg_4Al_{1.6}Ce_{0.4}$-HT280 system.

2.3. Catalytic Performance in VOC Oxidation

2.3.1. *n*-Butanol Oxidation

The catalytic performance of $Mg_4Al_{2-x}Ce_x$-HT280 and $Mg_4Al_{2-x}Ce_x$-HT500 materials was evaluated for butanol oxidation at temperatures ranging from 100 to 280 °C. The single carbon-containing product of butanol oxidation is CO_2 at high conversion levels. Butanal was identified as the primary intermediate product during the conversion of butanol to CO_2 with trace amounts of other aldehydes like propanal and ethanal detected. Figures 8–10 present, respectively, the total conversion of *n*-butanol, the conversion of butanol to CO_2 and the selectivity of butanal as a function of reaction temperature.

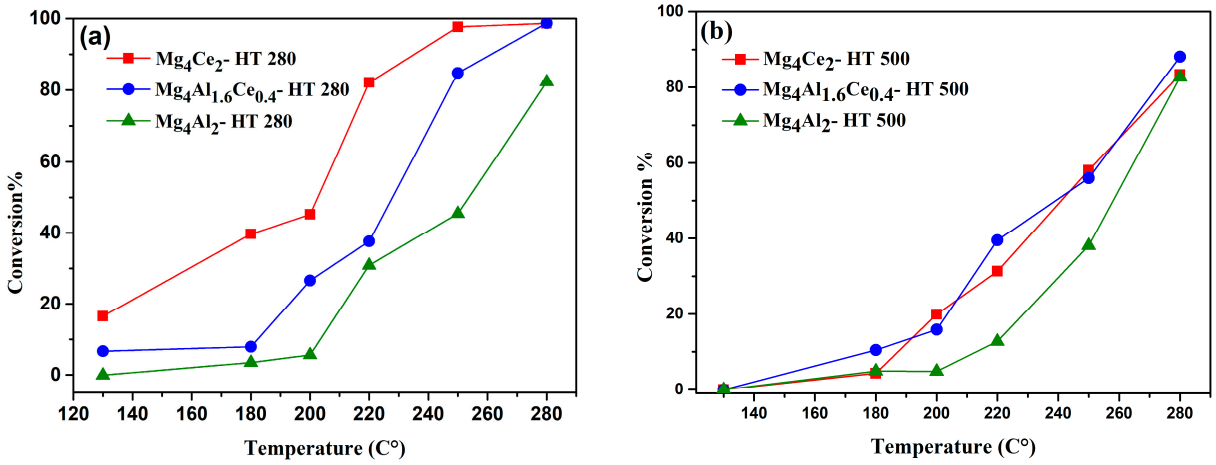

Figure 8. Butanol conversion versus temperature for the series: (**a**) $Mg_4Al_{2-x}Ce_x$-HT280 and (**b**) $Mg_4Al_{2-x}Ce_x$-HT500 (x = 0; 0.4 and 2).

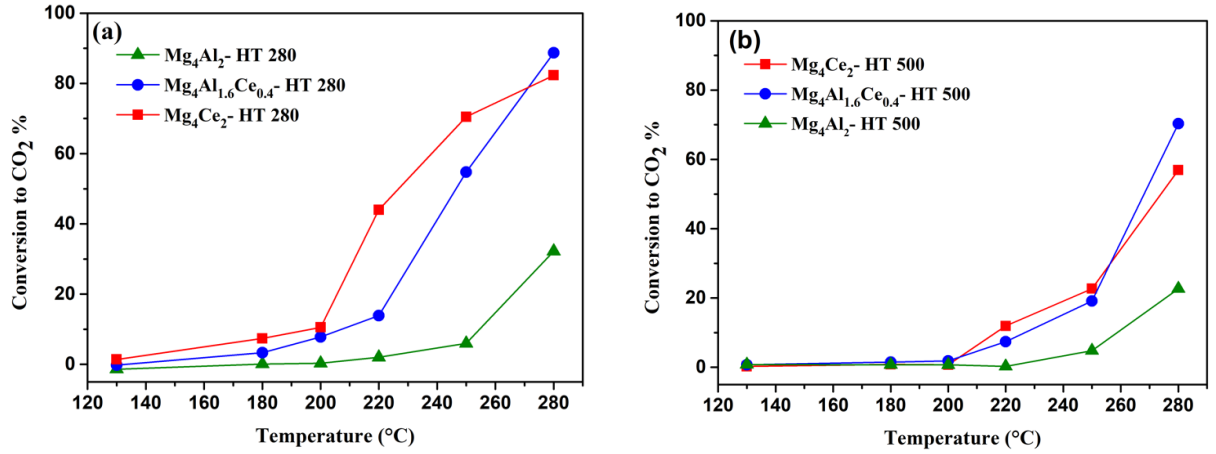

Figure 9. Conversion of butanol to CO_2 versus temperature for the series: (**a**) $Mg_4Al_{2-x}Ce_x$-HT280 and (**b**) $Mg_4Al_{2-x}Ce_x$-HT500 (x = 0; 0.4 and 2).

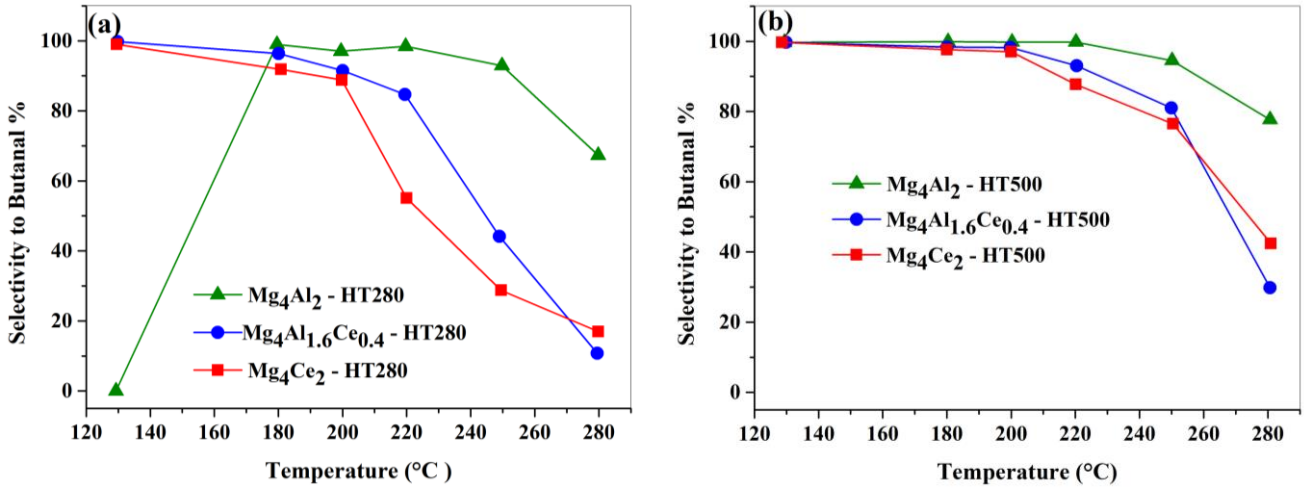

Figure 10. Selectivity to butanal versus temperature for the series: (**a**) $Mg_4Al_{2-x}Ce_x$-HT280 and (**b**) $Mg_4Al_{2-x}Ce_x$-HT500 (x = 0; 0.4 and 2).

In the absence of cerium, the Mg_4Al_2-HT catalyst, whatever its calcination temperature, exhibits a first phase of activity. It leads to a butanol conversion greater than 40% at 250 °C.

The observed reactivity of the Mg_4Al_2-HT catalyst is thought to be attributed to its basicity properties, which may be correlated to the mobility of oxygen species. Martin et al. [38] have explored this correlation in their preliminary investigation. The authors conducted measurements of the basicity of several oxides using CO_2 chemisorption, aiming to establish a relationship between surface basicity and oxygen surface mobility. Their findings indicate that an increase in oxide surface basicity and a decrease in the strength of the metal–oxygen bond lead to an enhanced rate of oxygen surface diffusion. Thus, oxygen mobility is associated with the presence of M^{n+}–O^{2-} bonds on the oxide surface, which determine the number and strength of basic sites at the solid's surface. Moreover, the basicity properties of hydrotalcite structure have long been recognized and are attributed to different types of surface basic sites, including strong basic sites in the form of O^{2-} ions, medium strong sites located near hydroxyl groups, and weak basic sites in the form of OH groups [39]. Lavalley et al. [40] showed that CO_2 adsorption on metal oxide surfaces generates different carbonate species that are indicative of the strength of the material's basicity. Weak basic sites are attributed to hydroxy groups on the catalyst's surface, while medium and strong sites are due to O^{2-} ions whose coordination depends on the metal–oxygen bond M^{n+}–O^{-}. Based on previous literature findings, we can infer that the basicity of our Mg_4Al_2-HT system is associated with the number of surface metal species, including Mg^{2+} and Al^{3+} [38]. The Al^{3+} cations in the MgAl structure are responsible for the appearance of hydroxy groups OH, which contributes to weak basicity [39]. Meanwhile, the Mg^{2+} cations coordinated to oxygen ions (Mg^{2+}–O^{2-}) give rise to oxygen species that exhibit medium basicity [39]. The choice of a basic pH value of 9.5 during catalyst preparation and the presence of Lewis acid/base sites (Mg–O and/or Al–O) could have a positive electronic effect on oxygen mobility [39,40]. This, in turn, can impact the activation of the butanol molecule. By considering the M^{n+}–O^{2-} couple and taking into account the electronegativity of the cation compared to that of the oxygen partner, the oxygen atom becomes less strongly bound, leading to increased mobility and facilitates its potential involvement in organic molecule reactions [40].

When partially substituting aluminum with cerium ($Mg_4Al_{1.6}Ce_{0.4}$-HT), the butanol conversion was significantly improved. It was observed in terms of activity and selectivity toward CO_2, which increased from 45% to 84% and from 5% to 55%, respectively, at 250 °C. This improvement was even more significant when the system was calcined at 280 °C. Additionally, the complete substitution of aluminum by cerium (Mg_4Ce_2-HT materials) confirmed the beneficial effect of cerium. In the case of the Mg_4Ce_2-HT280 sample, the conversion reached 100% with a conversion to CO_2 of around 80% at 250 °C.

The enhanced catalyst activity observed with higher cerium content could be attributed to various factors, such as the reducibility of cerium and/or the complexity of the material's basicity, which is influenced by the presence of multiple types of basic sites on the surface. Cerium on the surface of the catalyst may promote the formation of strong O^{2-} basic sites that could potentially displace and substitute the medium (Mg^{2+}–O^{2-}) and/or weak (Al^{3+}–O^{-}) basic sites on the surface.

Additionally, several studies have linked the activity of cerium-containing systems to their redox properties [38,39,41,42]. The presence of the Ce^{3+}/Ce^{4+} redox couple in the outer layers of the system creates electronic vacancies that facilitate the diffusion of O^{2-} species to the surface, resulting in their activation into nucleophilic species such as O^{2-}, O_2^{2-}, and O_2^{-} [39,41]. These reactive species are well known in the literature for their involvement in oxidation reactions [41].

Thus, the complex surface properties of the cerium-containing system during catalytic butanol oxidation are determined by both the basic nature and reducibility of the catalyst. Basicity enhances the acid–base interaction on the surface of the system, while reducibility increases the activity of the material.

Moreover, it is important to note that the Mg_4Al_2-HT, $Mg_4Al_{1.6}Ce_{0.4}$-HT, and Mg_4Ce_2-HT systems, all with an LDH structure (calcined at 280 °C), demonstrated excellent catalytic activity for the complete oxidation of butanol compared to their corresponding oxides

obtained after calcination at 500 °C. Among them, the solid Mg_4Ce_2-HT280, pretreated at 280 °C, had a total conversion of butanol with a conversion to CO_2 exceeding 82% at 250 °C. However, further increasing the calcination temperature was found to be unfavorable in improving the catalytic activity. A complete combustion of butanol took place on Mg_4Ce_2HT-500 until the temperature reached 280 °C. The same results are observed in a study on toluene oxidation over the OMS-2R catalyst pretreated at different temperatures by Sun et al. [43], Taking into account the characterization results (TPD and TGA results), the authors found that increasing the pretreated temperature from 250 to 500 °C led to a decrease in the activity toward combustion to CO_2. They suggested that the high calcination temperature resulted in a decreased capability for oxygen activation, which is essential in the redox mechanism of VOC oxidation. Many authors agree that the higher the oxygen mobility predicted, the better the catalytic activity in the VOC oxidation process, which can be performed by a redox mechanism, where the determining step is the removal of oxygen from the metallic oxide [43].

Based on both published research and our own experimental findings, it is possible to link the enhanced activity and, more specifically, CO_2 selectivity of the Mg_4Ce_2-HT system, especially when the hydrotalcite structure is conserved following pretreatment at 280 °C, to the structural, textural and redox properties of the solid. This distinguishes it from the other two systems studied, namely $Mg_4Al_{1.6}Ce_{0.4}$ and Mg_4Al_2. (i) The calcination of cerium-containing materials at 280 °C leads to the formation of diverse phases with distinct structures, including LDH Rhombohedral and cubic fluorite, as detected by XRD and Raman. Moreover, the stacking of LDH sheets with a homogenous mixture of cations at an atomic scale could improve the mobility of oxygen from the interior to the surface, resulting in better system activity. (ii) XPS analysis of the fresh Mg_4Ce_2HT-280 solid reveals the presence of Ce^{3+}/Ce^{4+} species on the surface. Following catalytic testing at 250 °C, the proportion of Ce^{3+} at the surface increases, indicating the greater reducibility of the system. These redox properties could promote the mobility of nucleophilic O^{2-}, $O_2{}^-$, $O_2{}^{2-}$, O^- oxygen species and consequently enhance the solid's activity. (iii) Additionally, the Mg_4Ce_2HT-280 system has a more homogeneous pore distribution compared to the other two systems. This texture can enhance the adsorption and desorption of reactants and products as well as facilitate the rapid regeneration of surface species.

2.3.2. Effect of Water Vapor on the Reactivity of Mg_4Ce_2HT-280 Material

To investigate the impact of water vapor on the catalytic performance of Mg_4Ce_2-HT280, a relative humidity of 33% was chosen, which corresponds to a stream of water vapor of 1.04 vol%. This value aligns with established practices in the literature [44,45]. Additionally, the selection of the Mg_4Ce_2-HT280 system was motivated by its superior activity, particularly in terms of butanol conversion to CO_2, compared to the other two systems.

Figure 11 shows that the presence of water vapor negatively affected the catalytic activity of Mg_4Ce_2-HT280 in butanol combustion with a slight shift of the butanol conversion profile toward higher temperatures, requiring 20 °C more for the same conversion observed in the absence of water vapor. It is worth noting that this shift is particularly prominent at low temperatures (<200 °C), which aligns with findings reported by Hu et al. [17]. The authors emphasized the significance of considering the impact of water vapor when conducting catalytic combustion at lower temperatures. Moreover, this inhibiting effect of water vapor on the activity of our system is not so marked; the low value of the relative humidity (33%) could be the cause of this result.

The literature suggests that water may act as a VOC oxidation inhibitor on several metal-based catalysts [44–47]. Based on the works of Li et al. [46] and Pan et al. [44], we attribute the decrease in catalytic activity to the competition between butanol and water molecules for adsorption on the active sites. This competition reduces the number of available active sites for butanol reaction, resulting in the observed decrease in the catalytic activity of Mg_4Ce_2HT-280.

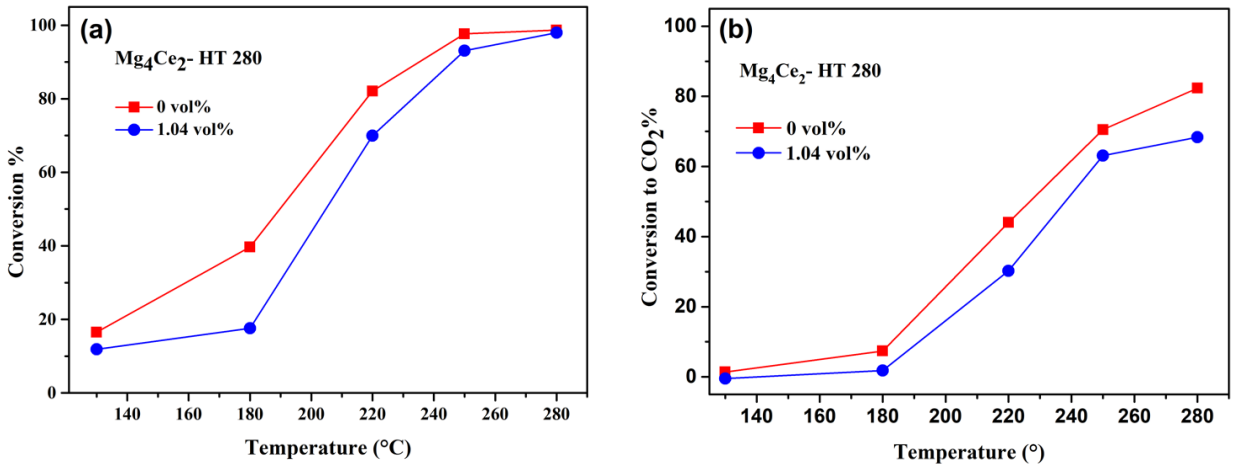

Figure 11. (**a**) Effect of water vapor in feed stream on the butanol conversion. (**b**) Effect of water vapor in feed stream on the conversion to CO_2.

2.3.3. Effect of *n*-Butanol/Ethyl Acetate Mixture on the Reactivity of Mg_4Ce_2HT-280 Material

The activity of Mg_4Ce_2HT-280 in the oxidation of *n*-butanol/ethyl acetate mixture was evaluated using a 1:1 molar ratio. The catalytic test results displayed in Figure 12 and Table 5 provides a comparison of the oxidation temperatures (T_{50} and T_{99}) for the individual components versus their mixture.

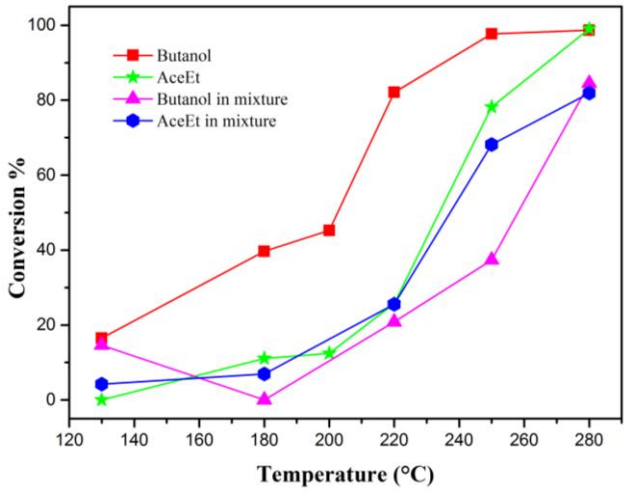

Figure 12. Evolution of *n*-butanol and ethyl acetate conversion, either alone or in a bi-component mixture, as a function of temperature over the Mg_4Ce_2-HT280 catalyst.

Table 5. Temperatures (°C) at which 50% and 99% of *n*-butanol, ethyl acetate alone or in bi-component mixture are converted.

Oxidized Compound	Compound in Mixture	Mg_4Ce_2-HT280	
		T_{50} (°C)	T_{99} (°C)
n-Butanol		205	250
Ethyl acetate		235	280
n-Butanol	Ethyl acetate	260	>280
Ethyl acetate	*n*-Butanol	240	>280

According to the data presented in Figure 12 and Table 5, when using the Mg_4Ce_2-HT280 system, the conversion profiles of single component reactions (butanol and ethyl

acetate) indicate that ethyl acetate is more resistant to oxidation than butanol. Specifically, the temperature required to achieve 50% and 99% conversion is approximately 30 °C higher for ethyl acetate than for butanol. It is important to note that during the oxidation of ethyl acetate, CO_2 is primarily produced, along with several by-products such as acetaldehyde, ethanol, and acetic acid, which depend on the reaction temperature.

The combustion behavior of a single component is different from that of the binary mixture of VOC. A mutual inhibiting effect is observed between the two compounds, with butanol combustion showing a more pronounced effect. Specifically, the presence of ethyl acetate in the reaction mixture significantly inhibits the rate of butanol oxidation, with conversion temperatures being higher by 50–60 °C than those observed when butanol is oxidized alone. On the other hand, the oxidation of ethyl acetate is only slightly inhibited by the presence of butanol.

Several researchers suggest that the inhibition effects could be due to competition between the compounds for adsorption sites [15,16,48,49] and/or for oxygen atoms [16]. The compound that is preferentially adsorbed is oxidized first [15]. In this particular case, ethyl acetate exhibits a stronger affinity with the catalyst surface and is therefore more strongly retained and adsorbed than butanol.

3. Experimental Section

3.1. Preparation of Mg-Al-Ce Mixed Oxides

A series of Mg-Al-Ce mixed oxides was prepared via the LDH route. The Mg–Al–Ce LDH precursors with a Mg:Al:Ce molar ratio of 4:2 − x:x (x = 0, 0.4, 0.8 and 2) were first prepared by the co-precipitation of corresponding nitrates ($Mg(NO_3)_2{\cdot}6H_2O$ (>99%), $Al(NO_3)_3{\cdot}9H_2O$ (>99%), $Ce(NO_3)_3{\cdot}6H_2O$ (>99.9%)) in an alkaline $NaOH/Na_2CO_3$ solution. An aqueous solution containing the nitrates was slowly added at room temperature to a vigorously stirred aqueous solution of NaOH (1 M) and Na_2CO_3 (1 M) until a final pH of 9.5 was achieved. The resulting slurry was heated at 60 °C with vigorous stirring for 15 h, and the resulting precipitate was filtered, washed five times with distilled water, and then dried at 80 °C for 24 h. The synthesized solids were calcined at 280 °C or 500 °C for 4 h in air.

3.2. Characterization Techniques and Methods

The nitrogen adsorption and desorption isotherms were performed at −196 °C on a Micromeritics ASAP 2010 apparatus (Norcross, Atlanta, GA, Micromeritics, USA), and the data were analyzed according the BET and BJH methods. Before starting the analysis, the samples were degassed at 150 °C in vacuum. The sample weight was about 500 mg.

Differential thermal and thermogravimetric analyses (DTA/TG) were carried out with a TA-Instrument SDT-2960 Thermobalance (New Castle, DE, USA). First, 10 to 15 mg of solid was heated at 5 °C/min up to 600 °C under air flow (100 $mL{\cdot}min^{-1}$).

The crystallinity of solids was determined at room temperature by X-Ray Diffraction (XRD) using a Bruker D8 Advance diffractometer (Bruker, Berlin, Germany) equipped with a copper anode (λ = 1.5406 Å). Patterns were acquired in the 2θ range 10–80° with a scanning rate of 0.02° and a count time of 2 s per step. The crystallite sizes of the hydrotalcite phase, cerium oxide, and magnesium oxide were estimated using Scherrer's equation for the (003), (111), and (200) reflections, respectively. The lattice parameter was estimated using the FullProf software (PANalytical, Malvern, Almelo, The Netherlands, 2018).

Laser Raman spectra (LRS) were recorded on Horiba Labram infinity laser Raman spectrometer (XY-DILOR) equipped with an optical multichannel charge-coupled device liquid nitrogen-cooled detector. The laser intensity (Ar+, 514.5 nm) was reduced by various filters (<1 mW), and the data were treated by the Lasbpec software. The spectral resolution and the accuracy in the Raman shifts are estimated to be 2 cm^{-1}. A tenth particle was examined for each sample to check its homogeneity.

X-ray photoelectron spectroscopy (XPS) was performed using AXIS Ultra DLD Kratos spectrometer equipped with a monochromatized aluminum source (Al Kα = 1486.6 eV).

Samples were preliminary degassed under an ultra-high vacuum (10^{-7} Torr) during one night. Post-reaction catalyst samples were sealed in their reactor tubes under He and transferred to a glove box under inert atmosphere. Samples were then loaded into the analysis chamber without exposure to atmospheric air. The binding energy (BE) was calibrated based on the line position of C 1s at 285 eV, which was assumed to be adventitious carbon. CasaXPS processing software was used to estimate the relative abundance of the different species.

3.3. Catalytic Experiments

The *n*-butanol oxidation was carried out in a Pyrex glass fixed-bed reactor under atmospheric pressure with a continuous flow system in the temperature range of 25–280 °C. The catalytic bed contained 100 mg of sample, and a space velocity (GHSV) of 15,789 h^{-1} was applied. The reaction mixture was generated by passing air at a flow rate of 100 mL/min through a saturator chamber filled with pure *n*-butanol, which was heated to 60 °C. The concentration of butanol was 800 ppm, which was controlled by the temperature of a homemade saturator and the additional air stream. All the lines were sufficiently heated at 120 °C to prevent the condensation of butanol and water in the tubes. The exit gases were analyzed using two gas chromatographs from Agilent Technologies (model 7890 A GC systems, CA, USA) with one equipped with an FID detector for analyzing organic compounds and the other equipped with a TCD detector for analyzing CO and CO_2 gases.

To achieve the oxidation of *n*-butanol and ethyl acetate mixture, two distinct saturators were employed for each VOC. The flow rate was maintained at 50 mL/min for each saturator. The mixture's composition was fixed at a 1:1 molar ratio, maintaining a feed composition of 1% in volume of total VOCs.

The oxidation process of *n*-butanol in the presence of water vapor involves the introduction of a water-filled saturator situated in a controlled bath, where the temperature is set at 26 °C. An air flow of 25 mL/min passes through the water-filled saturator, while the saturator containing pure *n*-butanol is traversed by a flow rate of 75 mL/min. The water vapor in the feed stream was 1.04 vol% corresponding to 33% of relative humidity. Mass flow meters are placed after each saturator to monitor the flow rates and prevent any potential gas backflow.

4. Conclusions

In this study, $Mg_4Al_{2-x}Ce_x$ LDHs were successfully synthesized by the co-precipitation method. Samples containing cerium exhibited interesting properties for the total oxidation reaction of *n*-butanol with the catalytic performance being more pronounced at high cerium content (Mg_4Ce_2-HT). The calcination of the solids at 280 °C maintained the stacking of the LDH structure and resulted in the highest catalytic activity compared to their corresponding oxide obtained after calcination at 500 °C. The significant improvement in catalytic activity and particularly the conversion to CO_2 with the Mg_4Ce_2-HT280 system, especially when the LDH structure is conserved, could be attributed to several factors. These include the homogeneous and regular distribution of active sites occupied by cerium in the LDH structure, the diversity of the phases obtained with different structures (LDH Rhombohedral and cubic fluorite), the presence of Ce^{3+}/Ce^{4+} species on the fresh surface solid, and the increase in Ce^{3+} proportion after the catalytic test, which indicated better reducibility of this system. Additionally, the Mg_4Ce_2HT-280 system presented a more homogeneous pore distribution compared to the other two systems, which could promote the adsorption and desorption of reactants and products as well as the rapid regeneration of surface species. All of these physico-chemical properties seem to be favorable to the activation and transformation of butanol into CO_2.

Moreover, in the presence of Mg_4Ce_2-HT 280 system, the addition of water vapor or ethyl acetate in the reaction mixture considerably inhibited the rate of butanol oxidation. This inhibitory effect could be caused by the competition between the butanol and water or ethyl acetate molecules for the adsorption sites and/or for the oxygen atoms.

Author Contributions: Conceptualization, methodology, visualization, supervision, writing—review and editing, N.H. and J.-F.L.; preparation and catalytic tests of materials F.S.; validation, formal analysis, investigation, F.S., N.H. and J.-F.L.; funding acquisition, N.H., C.R. and J.-F.L. All authors have read and agreed to the published version of the manuscript.

Funding: This research received no external funding.

Data Availability Statement: The data that support the findings of this study are available from the corresponding author upon reasonable request.

Acknowledgments: J.C. Morin, L. Burylo and O. Gardoll (UCCS) are acknowledged for discussions and Raman, XRD, ATG-ATD and BET-BJH experiments, respectively.

Conflicts of Interest: The authors declare no conflict of interest.

References

1. El Khawaja, R.; Veerapandian, S.K.P.; Rim Bitar, R.; De Geyter, N.; Rino Morent, R.; Heymans, N.; De Weireld, G.; Barakat, T.; Ding, Y.; Grêce, A.; et al. Boosting VOCs elimination by coupling different Techniques. *Chem. Synth.* **2022**, *2*, 13. [CrossRef]
2. Papaefthimiou, P.; Ioannides, T.; Verykios, X.E. VOC removal: Investigation of ethylacetate oxidation over supported Pt catalysts. *Catal. Today* **1999**, *54*, 81–92. [CrossRef]
3. Finol, M.F.; Rooke, J.; Su, B.L.; Trentesaux, M.; Giraudon, J.M.; Lamonier, J.F. Additional effects of Pt and Nb on hierarchically porous titania in the catalytic removal of n-butanol. *Catal. Today* **2012**, *192*, 154–159. [CrossRef]
4. Aggett, K.; Davies, T.E.; Morgan, D.J.; Hewes, D.; Taylor, S.T. The Influence of Precursor on the Preparation of CeO_2 Catalysts for the Total Oxidation of the Volatile Organic Compound Propane. *Catalysts* **2021**, *11*, 1461. [CrossRef]
5. Górecka, S.; Pacultová, K.; Fridrichová, D.; Górecki, K.; Bílková, T.; Žebrák, R.; Obalová, L. Catalytic Oxidation of Ammonia over Cerium-Modified Copper Aluminium Zinc Mixed Oxides. *Materials* **2021**, *14*, 6581. [CrossRef] [PubMed]
6. Pande, G.; Selvakumar, S.; Batra, V.S.; Gardoll, O.; Lamonier, J.F. Unburned carbon from bagasse fly ash as a support for a VOC oxidation catalyst. *Catal. Today* **2012**, *190*, 47–53. [CrossRef]
7. Valente, J.S.; Tzompantzi, F.; Prince, J. Highly efficient photocatalytic elimination of phenol and chlorinated phenols by CeO_2/MgAl layered double hydroxides. *Appl. Catal. B Environ.* **2011**, *102*, 276–285. [CrossRef]
8. Azalim, S.; Franco, M.; Brahmi, R.; Giraudon, J.M.; Lamonier, J.F. Removal of oxygenated volatile organic compounds by catalytic oxidation over Zr-Ce-Mn catalysts. *J. Hazard. Mater.* **2011**, *188*, 422–427. [CrossRef]
9. Blin, J.-L.; Michelin, L.; Lebeau, B.; Naydenov, A.; Velinova, R.; Kolev, H.; Gaudin, P.; Vidal, L.; Dotzeva, A.; Tenchev, K.; et al. Co–Ce Oxides Supported on SBA-15 for VOCs Oxidation. *Catalysts* **2021**, *11*, 366. [CrossRef]
10. Lu, X.; Xie, X.; Li, S.; Zhou, J.; Sun, W.; Xu, Y.; Sun, Y. Treatment of Purified Terephthalic Acid Waste water by Ozone Catalytic Oxidation Method. *Water* **2021**, *13*, 1906. [CrossRef]
11. Figueras, F.; Lopez, J.; Sanchez-Valente, J.; Vu, T.; Clacens, J.; Palomeque, J. Isophorone Isomerization as Model Reaction for the Characterization of Solid Bases: Application to the Determination of the Number of Sites. *J. Catal.* **2002**, *211*, 144–149. [CrossRef]
12. Wang, C.; Humayun, M.; Debecker, D.P.; Wu, C. Electrocatalytic water oxidation with layered double hydroxides confining single atoms. *Coord. Chem. Rev.* **2023**, *478*, 214973. [CrossRef]
13. Lim, A.M.H.; Yeo, J.W.; Zeng, H.C. Preparation of CuZn-Doped MgAl-Layered Double Hydroxide Catalysts through the Memory Effect of Hydrotalcite for Effective Hydrogenation of CO_2 to Methanol. *ACS Appl. Energy Mater.* **2023**, *6*, 782–794. [CrossRef]
14. Das, J.; Das, D.; Parida, K.M. Preparation and characterization of Mg-Al hydrotalcite-like compounds containing cerium. *J. Colloid Interface Sci.* **2006**, *301*, 569–574. [CrossRef]
15. Aguero, F.N.; Barbero, B.P.; Gambaro, L.; Cadús, L.E. Catalytic combustion of volatile organic compounds in binary mixtures over MnO_x/Al_2O_3 catalyst. *Appl. Catal. B Environ.* **2009**, *91*, 108–112. [CrossRef]
16. Santos, V.P.; Pereira, M.F.R.; Órfão, J.J.M.; Figueiredo, J.L. Mixture effects during the oxidation of toluene, ethyl acetate and ethanol over a cryptomelane catalyst. *J. Hazard. Mater.* **2011**, *185*, 1236–1240. [CrossRef]
17. Hu, J.; Li, W.B.; Liu, R.F. Highly efficient copper-doped manganese oxide nanorod catalysts derived from CuMnO hierarchical nanowire for catalytic combustion of VOCs. *Catal. Today* **2018**, *314*, 147–153. [CrossRef]
18. Azalim, S.; Brahmi, R.; Agunaou, M.; Beaurain, A.; Giraudon, J.M.; Lamonier, J.F. Washcoating of cordierite honeycomb with Ce-Zr-Mn mixed oxides for VOC catalytic oxidation. *Chem. Eng. J.* **2013**, *223*, 536–546. [CrossRef]
19. Papaefthimiou, P.; Ioannides, T.; Verykios, X.E. Combustion of non-halogenated volatile organic compounds over group VIII metal catalysts. *Appl. Catal. B* **1997**, *13*, 175–184. [CrossRef]
20. Papaefthimiou, P.; Ioannides, T.; Verykios, X.E. Catalytic incineration of volatile organic compounds present in industrial waste streams. *Appl. Therm. Eng.* **1998**, *18*, 1005–1012. [CrossRef]
21. Yu, X.; Deng, J.; Liu, Y.; Jing, L.; Gao, R.; Hou, Z.; Zhang, Z.; Dai, H. Enhanced Water Resistance and Catalytic Performance of Ru/TiO_2 by Regulating Brønsted Acid and Oxygen Vacancy for the Oxidative Removal of 1,2-Dichloroethane and Toluene. *Environ. Sci. Technol.* **2022**, *56*, 11739–11749. [CrossRef]
22. Pérez, A.; Lamonier, J.F.; Giraudon, J.M.; Molina, R.; Moreno, S. Catalytic activity of Co-Mg mixed oxides in the VOC oxidation: Effects of ultrasonic assisted in the synthesis. *Catal. Today* **2011**, *176*, 286–291. [CrossRef]

23. Zhitova, E.S.; Sheveleva, R.M.; Kasatkin, A.V.; Zolotarev, A.A.; Bocharov, V.N.; Anastasia, N.; Kupchinenko, A.N.; Dmitry, I.; Belakovsky, D.I. Crystal Structure of Hydrotalcite Group Mineral—Desautelsite, $Mg_6Mn^{III}_2(OH)_{16}(CO_3)\cdot 4H_2O$, and Relationship between Cation Size and In-Plane Unit Cell Parameter. *Symmetry* **2023**, *15*, 1029. [CrossRef]
24. Pérez-Ramírez, J.; Mul, G.; Kapteijn, F.; Moulijn, J.A. In situ investigation of the thermal decomposition of Co-Al hydrotalcite in different atmospheres. *J. Mater. Chem.* **2001**, *11*, 821–830. [CrossRef]
25. Wagassa, A.N.; Tufa, L.T.; Lee, J.; Zereffa, E.A.; Shifa, T.A. Controllable Doping of Mn into $Ni_{0.075-x}Mn_xAl_{0.025}(OH)_2(CO_3)_{0.0125}\cdot yH_2O$ for Efficient Adsorption of Fluoride Ions. *Glob. Chall.* **2023**, *7*, 2300018. [CrossRef] [PubMed]
26. Mora, M.; Jiménez-Sanchidrián, C.; Rafael Ruiz, J. Raman spectroscopy study of layered-double hydroxides containing magnesium and trivalent metals. *Mater. Lett.* **2014**, *120*, 193–195. [CrossRef]
27. Pérez-Ramírez, J.; Mul, G.; Moulijn, J.A. In situ Fourier transform infrared and laser Raman spectroscopic study of the thermal decomposition of Co-Al and Ni-Al hydrotalcites. *Vib. Spectrosc.* **2001**, *27*, 75–88. [CrossRef]
28. Palmer, S.J.; Frost, R.L.; Spratt, H.J. Synthesis and Raman spectroscopic study of Mg/Al, Fe hydrotalcites with variable cationic ratios. *J. Raman Spectrosc.* **2009**, *40*, 1138–1143. [CrossRef]
29. Cwele, T.; Mahadevaiah, N.; Singh, S.; Friedrich, H.B. Effect of Cu additives on the performance of a cobalt substituted ceria ($Ce_{0.90}Co_{0.10}O_{2-\delta}$) catalyst in total and preferential CO oxidation. *Appl. Catal. B Environ.* **2016**, *182*, 1–14. [CrossRef]
30. Sudarsanam, P.; Mallesham, B.; Reddy, P.S.; Großmann, D.; Grünert, W.; Reddy, B.M. Nano-Au/CeO_2 catalysts for CO oxidation: Influence of dopants (Fe, La and Zr) on the physicochemical properties and catalytic activity. *Appl. Catal. B Environ.* **2014**, *144*, 900–908. [CrossRef]
31. Kloprogge, J.T.; Frost, R.L. Infrared emission spectroscopic study of the thermal transformation of Mg-, Ni- and Co-hydrotalcite catalysts. *Appl. Catal. A Gen.* **1999**, *184*, 61–71. [CrossRef]
32. Millange, F.; Walton, R.I.; O'Hare, D. Time-resolved in situ X-ray diffraction study of the liquid-phase reconstructitm of Mg-Al-carboaate hydrotalcite-like compounds. *J. Mater. Chem.* **2000**, *10*, 1713–1720. [CrossRef]
33. Lamonier, J.F.; Boutoundou, A.B.; Gennequin, C.; Pérez-Zurita, M.J.; Siffert, S.; Aboukais, A. Catalytic removal of toluene in air over Co-Mn-Al nano-oxides synthesized by hydrotalcite route. *Catal. Lett.* **2007**, *118*, 165–172. [CrossRef]
34. Zhang, W.H.; Guo, X.D.; He, J.; Qian, Z.Y. Preparation of Ni(II)/Ti(IV) Layered Double Hydroxide at High Supersaturation. *J. Eur. Ceram. Soc.* **2008**, *28*, 1623–1629. [CrossRef]
35. Machida, M.; Uto, M.; Kurogi, D.; Kijima, T. MnO(x)-CeO_2 binary oxides for catalytic NO(x) sorption at low temperatures. Sorptive removal of NO(x). *Chem. Mater.* **2000**, *12*, 3158–3164. [CrossRef]
36. Larachi, F.; Pierre, J.; Adnot, A.; Bernis, A. Ce 3d XPS study of composite $Ce_xMn_{1-x}O_{2-y}$ wet oxidation catalysts. *Appl. Surf. Sci.* **2002**, *195*, 236–250. [CrossRef]
37. Shyu, J.Z.; Weber, W.H.; Gandhi, H.S. Surface characterization of alumina-supported ceria. *J. Phys. Chem.* **1988**, *92*, 4964–4970. [CrossRef]
38. Martin, D.; Duprez, D. Mobility of surface species on oxides. 1. isotopic exchange of $18O_2$ with 16O of SiO_2, AI_2O_3, ZrO_2, MgO, CeO_2, and CeO_2-Al_2O_3. activation by noble metals. correlation with oxide basicity. *J. Phys. Chem.* **1996**, *100*, 9429–9438. [CrossRef]
39. Melang Me Nze, V.; Fontaine, C.; Barbier, J. Synthèse et caractérisation d'oxydes mixtes de type MgAlCe pour l'oxydation catalytique de l'acide acétique. *C. R. Chim.* **2017**, *20*, 67–77. [CrossRef]
40. Lavalley, J.C. Infrared spectrometric studies of the surface basicity of metal oxides and zeolites using adsorbed probe molecules. *Catal. Today* **1996**, *27*, 377–401. [CrossRef]
41. Bordes-Richard, É. Les défis en catalyse hétérogène. *L'Actual. Chim.* **2002**, *5–6*, 38–44.
42. Knözinger, H.; Ratnasamy, P. Science and Engineering, Catalytic Aluminas: Surface Models and Characterization of surface sites. *Catal. Rev.* **1978**, *17*, 31–70. [CrossRef]
43. Sun, H.; Chen, S.; Wang, P.; Quan, X. Catalytic oxidation of toluene over manganese oxide octahedral molecular sieves (OMS-2) synthesized by different methods. *Chem. Eng. J.* **2011**, *178*, 191–196. [CrossRef]
44. Pan, H.; Xu, M.; Li, Z.; Huang, S.; He, C. Catalytic combustion of styrene over copper based catalyst: Inhibitory effect of water vapor. *Chemosphere* **2009**, *76*, 721–726. [CrossRef]
45. Kikuchi, R.; Maeda, S.; Sasaki, K.; Wennerström, S.; Eguchi, K. Low-temperature methane oxidation over oxide-supported Pd catalysts: Inhibitory effect of water vapor. *Appl. Catal. A Gen.* **2002**, *232*, 23–28. [CrossRef]
46. Li, X.; Wang, L.; Xia, Q.; Liu, Z.; Li, Z. Catalytic oxidation of toluene over copper and manganese based catalysts: Effect of water vapor. *Catal. Commun.* **2011**, *14*, 15–19.
47. Musialik-Piotrowska, A.; Syczewska, K. Combustion of volatile organic compounds in two-component mixtures over monolithic perovskite catalysts. *Catal. Today* **2000**, *59*, 269–278.
48. Blasin-Aubé, V.; Belkouch, J.; Monceaux, L. General study of catalytic oxidation of various VOCs over $La_{0.8}Sr_{0.2}MnO_{3+x}$ perovskite catalyst—Influence of mixture. *Appl. Catal. B Environ.* **2003**, *43*, 175–186.
49. Mazzarino, I.; Barresi, A.A. Catalytic combustion of voc mixtures in a monolithic reactor. *Catal. Today* **1993**, *17*, 335–347. [CrossRef]